JACS Au
AN OPEN ACCESS JOURNAL OF THE AMERICAN CHEMICAL SOCIETY

pubs.acs.org/jacsau Letter

Enhanced NH_3 Synthesis from Air in a Plasma Tandem-Electrocatalysis System Using Plasma-Engraved N-Doped Defective MoS_2

Jiageng Zheng,[#] Hao Zhang,[*,#] Jiabao Lv, Meng Zhang, Jieying Wan, Nick Gerrits, Angjian Wu, Bingru Lan, Weitao Wang, Shuangyin Wang,[*] Xin Tu,[*] Annemie Bogaerts,[*] and Xiaodong Li

Cite This: *JACS Au* 2023, 3, 1328−1336 Read Online

ACCESS | Metrics & More | Article Recommendations | Supporting Information

ABSTRACT: We have developed a sustainable method to produce NH_3 directly from air using a plasma tandem-electrocatalysis system that operates via the N_2−NO_x−NH_3 pathway. To efficiently reduce NO_2^- to NH_3, we propose a novel electrocatalyst consisting of defective N-doped molybdenum sulfide nanosheets on vertical graphene arrays (N-MoS_2/VGs). We used a plasma engraving process to form the metallic 1T phase, N doping, and S vacancies in the electrocatalyst simultaneously. Our system exhibited a remarkable NH_3 production rate of 7.3 mg h^{-1} cm^{-2} at −0.53 V vs RHE, which is almost 100 times higher than the state-of-the-art electrochemical nitrogen reduction reaction and more than double that of other hybrid systems. Moreover, a low energy consumption of only 2.4 MJ $mol_{NH_3}^{-1}$ was achieved in this study. Density functional theory calculations revealed that S vacancies and doped N atoms play a dominant role in the selective reduction of NO_2^- to NH_3. This study opens up new avenues for efficient NH_3 production using cascade systems.

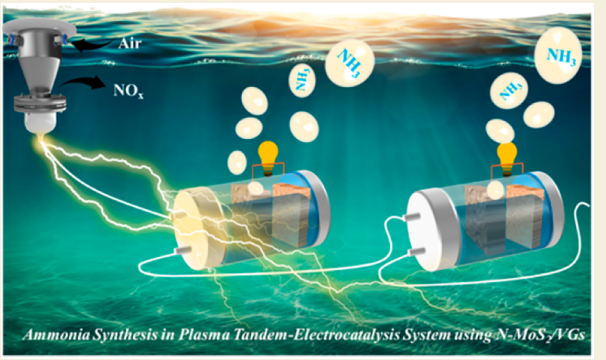

KEYWORDS: *sustainable NH_3 production, plasma electrocatalysis, defective N-MoS_2, plasma engraving, density functional theory*

INTRODUCTION

Ammonia (NH_3) is essential for modern agriculture[1,2] and is being explored as a promising carbon-free hydrogen carrier to tackle climate change and energy challenges.[3] However, the conventional centralized Haber−Bosch process for industrial NH_3 production requires extremely harsh conditions,[4] resulting in high energy demands[5] and significant CO_2 emissions.[6] Therefore, developing sustainable, environmentally friendly, and distributable routes for NH_3 production is critical.

One promising approach is electrochemical nitrogen reduction reaction (eNRR) to NH_3, which can be powered by renewable electricity using abundant N_2/air and H_2O under ambient conditions.[7−11] The performance of electrocatalysts is crucial for eNRR kinetics. Among the noble-metal-based,[12,13] transition-metal-based,[14,15] and metal-free electrocatalysts[16,17] explored, Mo, especially MoS_2, is of particular interest due to its natural occurrence in biological nitrogen fixation and structural similarity to nitrogenase.[18−21] Recently, there has been a surge in efforts to enhance catalyst reactivity through phase transformation,[22] heteroatom doping,[23] and defect engineering.[24] Nevertheless, the ultrastrong N≡N bond,[25−27] competitive hydrogen evolution reaction (HER),[28] and poor solubility of N_2 in the electrolyte[29] have limited the NH_3 production rate to <0.1 mg h^{-1} cm^{-2}.

To address these challenges, a promising two-step strategy has been proposed that uses plasma to activate inert N_2 into more accessible and clean nitrogen oxides (NO_x), followed by enhanced electroreduction of NO_x^- into NH_3.[30−32] Although NO_x^- may be abundant in wastewater, it would be unsuitable for this application due to the presence of impurities. The plasma electrocatalysis approach uses air instead of pure nitrogen, eliminating the need for energy-intensive air separation and purification processes, and is suitable for intermittent and decentralized operation using renewable energy sources as a turnkey process.[33−35] While an NH_3 production rate of up to 3.0 mg h^{-1} cm^{-2} has been achieved,[36,37] investigations into this strategy remain extremely limited. Further development of new electrochemical NO_x reduction reaction (eNO_x^-RR) processes, including system design and high-performance catalysts such as MoS_2, is critical to improve the slow conversion of NO_x^- to NH_3 in the second

Received: February 20, 2023
Revised: April 12, 2023
Accepted: April 13, 2023
Published: April 26, 2023

https://doi.org/10.1021/jacsau.3c00087
JACS Au 2023, 3, 1328−1336

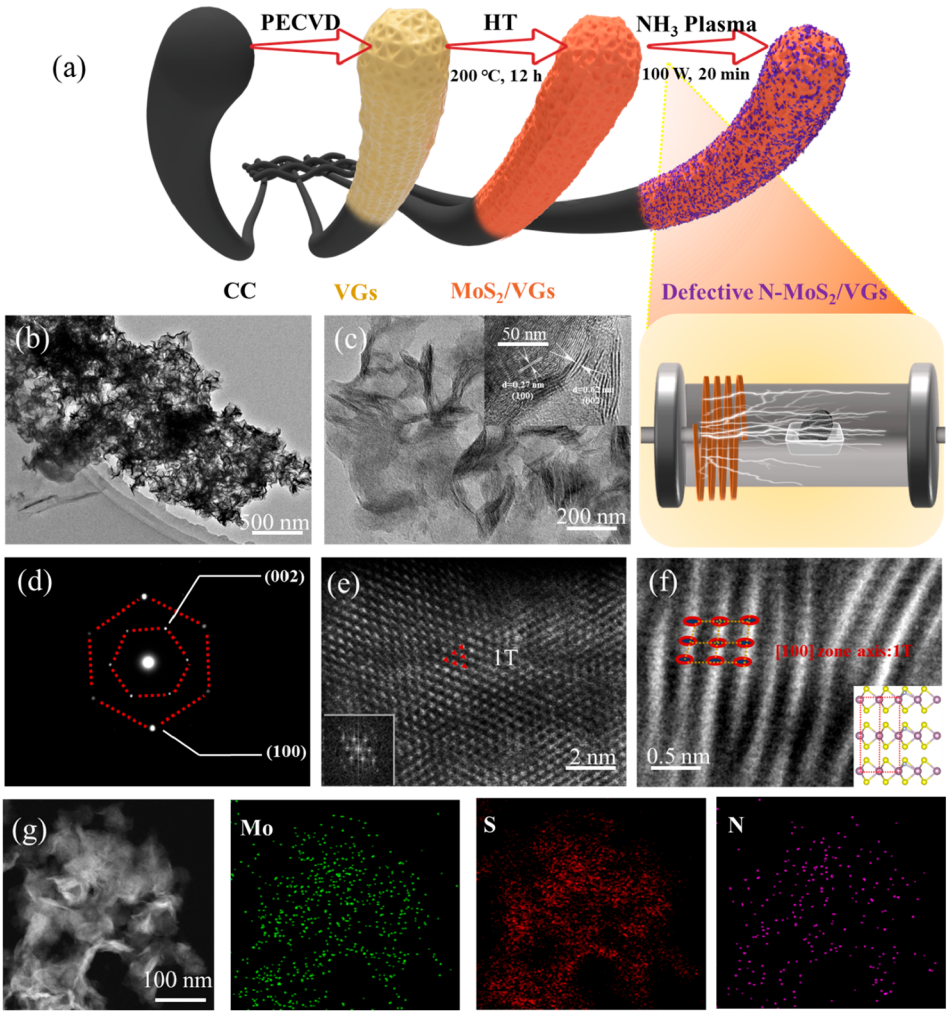

Figure 1. (a) Schematic illustration for N-MoS_2/VGs fabrication procedure and RF NH_3 plasma engraving process. (b) TEM image, (c) HRTEM image, (d) SAED pattern, (e) HAADF image, (f) AC-STEM image, and (g) EDX mapping of N-MoS_2/VGs.

step. Moreover, existing catalyst engineering strategies typically require high temperature (>300 °C)[38] and long-duration treatment (>2 h),[24] calling for a more facile and rational catalyst fabrication approach. Furthermore, a molecular-level understanding of the complex eNO_x^-RR mechanism remains limited, requiring in-depth experimental and theoretical studies.

Herein we propose a plasma tandem-electrocatalysis system to generate NH_3 from air (see Plasma Tandem-Electrocatalysis Setup and Figure S1). We engineered a novel defective N-MoS_2 electrocatalyst supported by vertical graphene arrays on carbon cloth (VGs/CC) with exceptional eNO_x^-RR reactivity. Advanced physical characterizations and density functional theory (DFT) calculations were conducted to elucidate the eNO_x^-RR reaction pathways with N-MoS_2/VGs.

RESULTS AND DISCUSSION

The MoS_2 nanosheets were assembled by a hydrothermal (HT) method and supported by vertical graphene arrays obtained through plasma-enhanced chemical vapor deposition (PECVD) on CC (Figure 1a and Catalyst Synthesis). The transmission electron microscopy (TEM) image (Figure 1b) confirmed the formation of a well-defined nanosheet profile. The marked space lattice fringe and distinct spots in the high-resolution transmission electron microscopy (HRTEM) image (Figure 1c) together with the selected-area electron diffraction (SAED) pattern (Figure 1d) revealed the (002) and (100) planes of MoS_2.

Notably, we pioneered a radiofrequency (RF) NH_3 plasma strategy for atomic-level surface engineering of MoS_2 (Figure 1a). By creation of a plasma sheath on the sample surface, ablated Mo atoms reacted with N atoms in the plasma to form N-MoS_2. Furthermore, the plasma treatment also generated crystal vacancies via ion sputtering and etching effects of NH_3.[39−41] This method required only a short duration (20 min) and low temperature (25 °C). The formation of octahedrally coordinated 1T-MoS_2 after the plasma engraving was confirmed by high-angle annular dark-field (HAADF) (Figure 1e) and spherical aberration corrected scanning transmission electron microscopy (AC-STEM) along the (100) zone axis (Figure 1f). The HRTEM images of MoS_2/VGs and N-MoS_2/VGs further evidenced the distinct phase transformation from 2H to 1T (Figures S2 and S3). Additionally, energy-dispersive X-ray (EDX) elemental mapping images demonstrated the uniform distribution of Mo, S, and N in the N-MoS_2/VGs (Figure 1g).

X-ray diffraction (XRD) patterns (Figure 2a) reveal characteristic peaks at 14.37°, 32.68°, and 39.54° that

https://doi.org/10.1021/jacsau.3c00087
JACS Au 2023, 3, 1328−1336

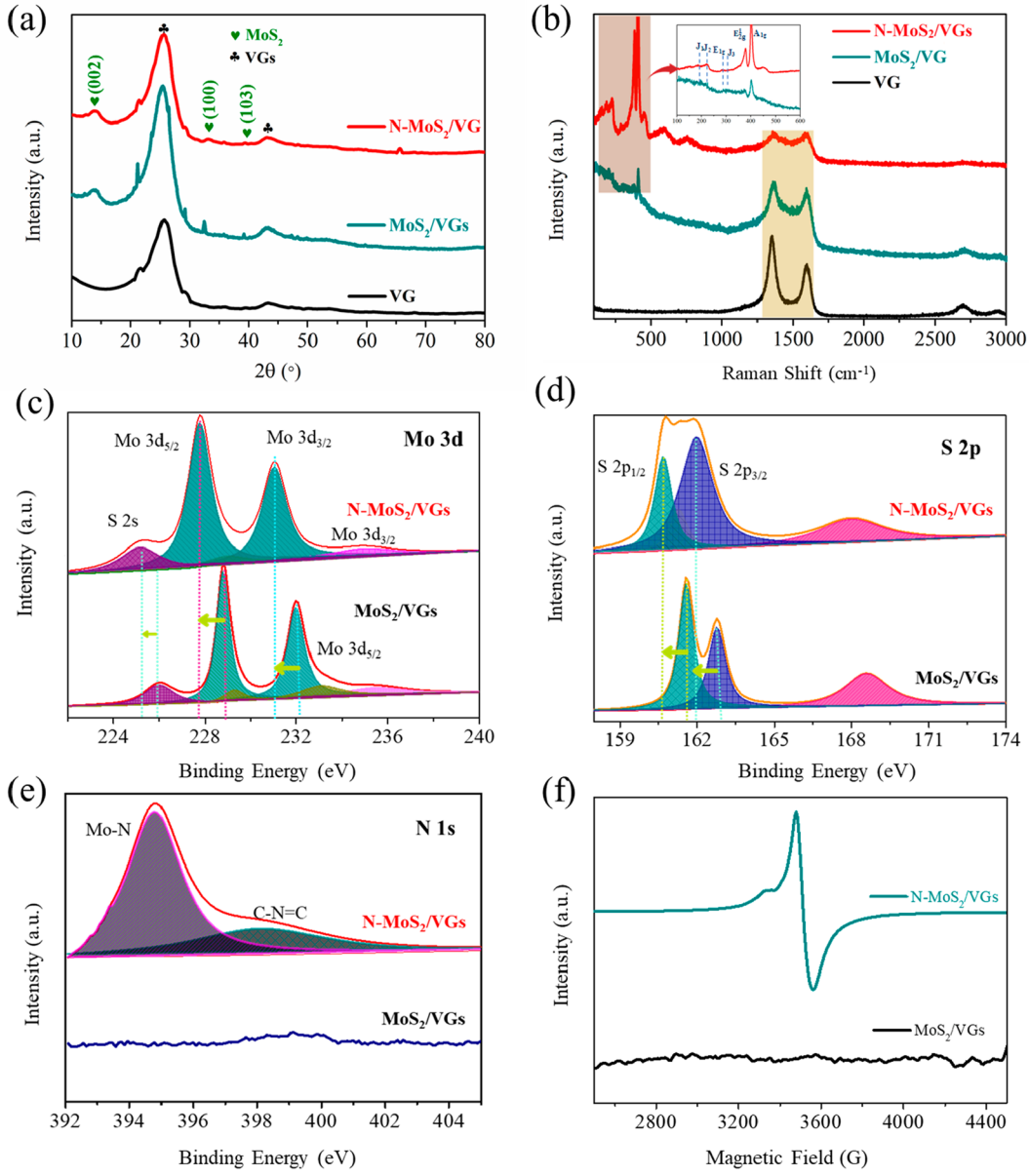

Figure 2. (a) XRD patterns and (b) Raman spectra of N-MoS_2/VGs, MoS_2/VGs, and VGs. (c–e) XPS spectra of (c) Mo 3d, (d) S 2p, and (e) N 1s over N-MoS_2/VGs and MoS_2/VGs. (f) EPR spectra of N-MoS_2/VGs and MoS_2/VGs.

correspond to the (002), (100), and (103) planes of MoS_2 (PDF no. 37-1492) for N-MoS_2/VGs, MoS_2/VGs, and VGs. The 1T phase of N-MoS_2/VGs is further confirmed by Raman spectroscopy (Figure 2b). The E_{2g} and A_{1g} peaks at 380 and 405 cm^{-1}, respectively, are observed in both MoS_2/VGs and N-MoS_2/VGs, with N-MoS_2/VGs also exhibiting three additional peaks (148, 207, and 335 cm^{-1}) associated with vibrational modes of the 1T phase. The E_{2g} peak (380 cm^{-1}) is also found in N-MoS_2/VGs due to the well-organized tetragonal symmetry.[42−44] X-ray photoelectron spectroscopy (XPS) (Figure 2c–e) revealed the presence of Mo, S, and N in N-MoS_2/VGs and the absence of N in MoS_2/VGs. The Mo 3d spectrum of MoS_2/VGs can be deconvoluted into four peaks, with two dominant peaks at 232.0 eV (Mo $3d_{3/2}$) and 229.1 eV (Mo $3d_{5/2}$) assigned to the 1T phase and two other peaks at 233.5 eV (Mo $3d_{3/2}$) and 229.6 eV (Mo $3d_{5/2}$) allocated to the 2H phase.[45,46] Conversely, only two typical 1T phase peaks at 231.2 eV (Mo $3d_{3/2}$) and 229.1 eV (Mo $3d_{5/2}$) are detected in N-MoS_2/VGs. Furthermore, the positive shift of N-MoS_2/VGs to MoS_2/VGs also confirms the phase transformation from 2H to 1T. Notably, the S:Mo ratio decreased from 1.74 to 1.37, according to quantized EDX data (Table S1), likely due to the substitution of N and possible S vacancies induced by plasma engraving. This hypothesis is explicitly proven by the electron paramagnetic resonance (EPR) spectroscopy results (Figure 2f), which display a prominent signal at $g = 2.004$ assigned to S vacancies in N-MoS_2/VGs and no signal in MoS_2/VGs, suggesting the partial deletion of thiol–Mo bonds in N-MoS_2/VGs.[47]

Comparative experiments in the plasma or electrocatalysis alone system and the plasma electrocatalysis system with different catalysts were performed at −0.33 V versus reversible hydrogen electrode (V vs RHE). As shown in Figure 3a, neither the plasma- or electrocatalysis-alone system nor the eNO_x^-RR over the substrates (CC and VGs/CC) yielded significant NH_3. However, the MoS_2 catalyst dramatically

https://doi.org/10.1021/jacsau.3c00087
JACS Au 2023, 3, 1328−1336

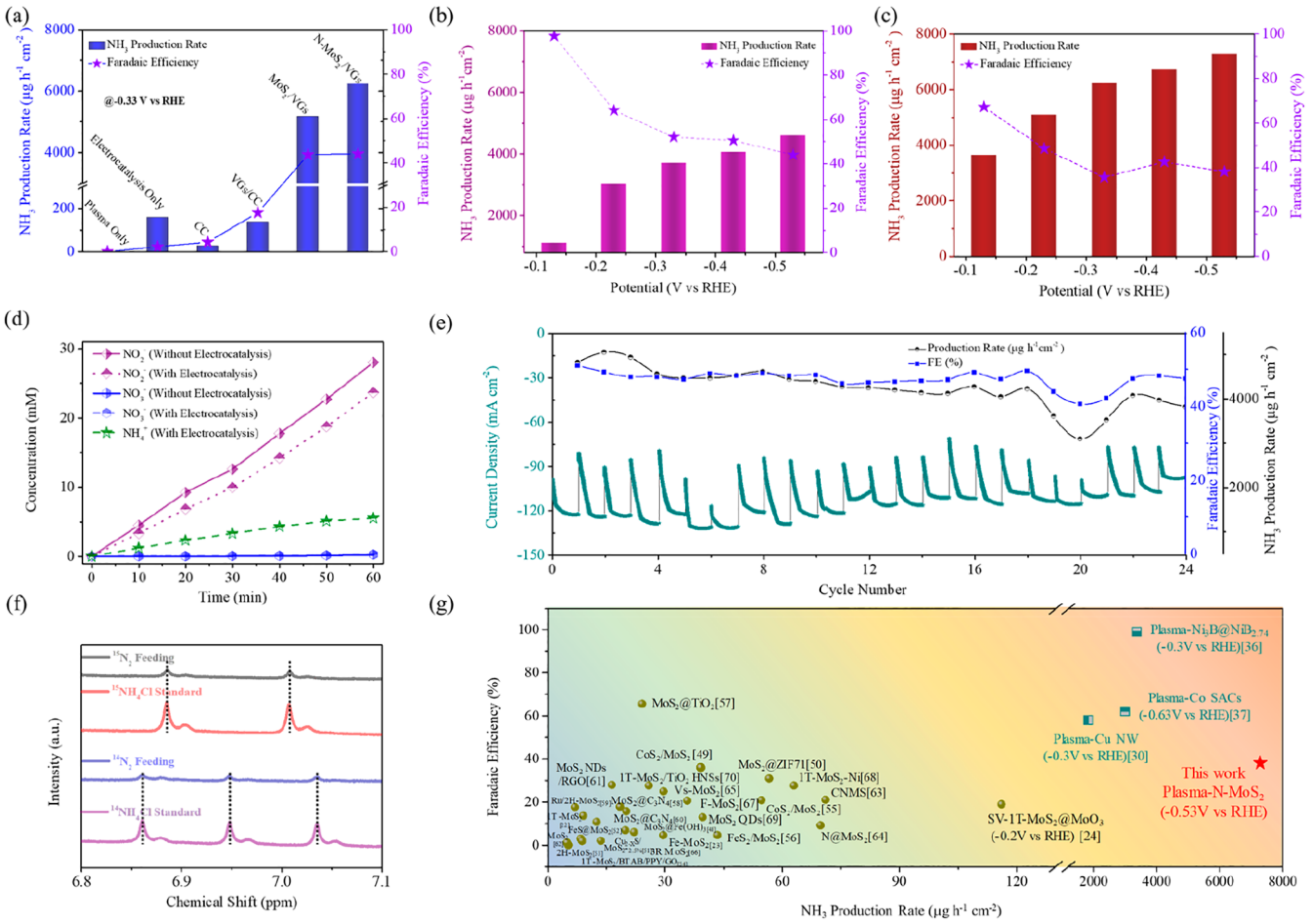

Figure 3. (a–c) NH_3 production rates and FEs for (a) plasma only, N-MoS_2/VGs electrocatalysis only, and plasma electrocatalysis with different catalysts, (b) plasma single-electrocatalysis, and (c) plasma tandem-electrocatalysis. (d) Time-dependent concentrations of nitrate, nitrite, and NH_4^+ with/without electrocatalysis in the hybrid system. (e) Stability tests. (f) ^1H NMR (600 MHz) spectra in $^{14}N_2$ or $^{15}N_2$ atmosphere after N-MoS_2/VGs electrocatalysis. (g) Comparison of eNRR using different MoS_2 catalysts (green symbols), other plasma-electrocatalysis systems (indigo symbols), and this work (red star). See Tables S6 and S7 for more details.

enhanced the NH_3 production rate (5.2 mg h^{-1} cm^{-2}) by a factor of approximately 38 over the substrates. Notably, the defective N-MoS_2/VGs catalyst further improved the catalytic reactivity by over 20%, reaching a production rate of up to 6.2 mg h^{-1} cm^{-2}. This enhancement is attributed to the improved electron conductivity, higher charge polarization, and increased active sites of N-MoS_2/VGs, as discussed above.

In this study, plasma tandem-electrocatalysis was utilized by coupling double electrocatalyst cells, and for comparison, a plasma single-electrocatalysis system was also tested. The results, depicted in Figure 3b,c, demonstrated that increasing potentials had a positive effect on the average NH_3 production rate but had a negative impact on the Faradaic efficiency (FE) in both modes. A maximum production rate of 4.6 mg h^{-1} cm^{-2} (FE = 44%) and a highest FE of 97.6% (NH_3 production = 1.12 mg h^{-1} cm^{-2}) were achieved, respectively, at −0.53 and −0.13 V vs RHE in the single-electrocatalysis mode. The tandem-electrocatalysis system significantly increased the production rate to 7.3 mg h^{-1} cm^{-2} (FE = 38.1%) at −0.53 V vs RHE (Figure 3c) (see Figures S6–S10 for more comparative results).

The air plasma produced a substantial NO_x concentration (up to 1.87% with NO:NO_2 ≈ 5:1) for subsequent eNO_x^-RR process. To elucidate the origin of NH_3 in eNO_x^-RR, we measured the concentrations of NO_2^-, NO_3^-, and NH_4^+ in the electrolyte during plasma discharge with and without electrocatalysis. NO_2^- was found to be the dominant NO_x^- (Figure 3d) with a formation rate of 28 mM h^{-1}, and it was significantly consumed in the presence of electrocatalysis, strongly indicating that NH_3 is primarily produced from NO_2^- (referred to as eNO_2^-RR hereafter).

The catalyst stability was validated by successive repetitive (24 times in 24 h) tests at −0.33 V vs RHE (Figure 3e). The scanning electron microscopy (SEM) images of the N-MoS_2/VGs catalyst before and after stability tests revealed no noticeable morphological changes (Figure S13). To confirm the origin of nitrogen for the produced NH_3, we conducted an isotopic labeling experiment using $^{15}N_2$. Consistent with the standard sample, the spectra in Figure 3f exhibited two and three characteristic peaks indexed to $^{15}NH_4^+$ and $^{14}NH_4^+$. Moreover, their production rates determined by NMR spectroscopy exhibited insignificant differences (Figure S14), excluding the influence of the surroundings. Remarkably, the system achieved a maximum NH_3 production rate of 7.3 mg h^{-1} cm^{-2}, which is almost 100 times higher than that of state-of-the-art MoS_2 eNRR[22−24,48−70] and over 2 times better than that of other hybrid systems (Figure 3g).[30,36,37]

https://doi.org/10.1021/jacsau.3c00087
JACS Au 2023, 3, 1328−1336

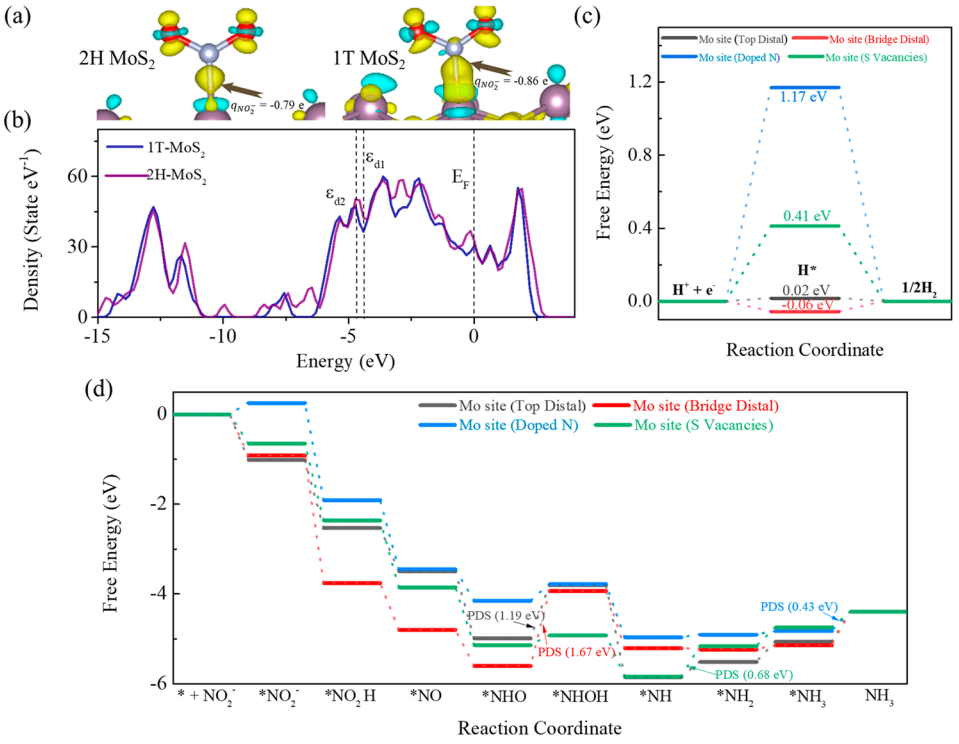

Figure 4. (a) Differential charge densities of adsorbed NO_2^- on 1T-MoS_2 and 2H-MoS_2. (b) DOS plots of 1T-MoS_2 and 2H-MoS_2. (c) HER and (d) NRR Gibbs free energy diagrams on various adsorption sites.

Moreover, we conducted DFT calculations to elucidate the enhanced eNO_2^-RR kinetics of the N-MoS_2 system (see Section S-VII-1 in the Supporting Information (SI) for details). Our simulation model (Figure S15) featured N-MoS_2(100) with S vacancies, which correlated with the catalyst characterization results. Figures 4a, S16, and S17 illustrate significant differences in the differential charge density of adsorbed NO_2^- on 2H and 1T phases of MoS_2. In the 1T phase, the electron accumulation (yellow areas) and electron loss (blue areas) are more extensive, reflecting greater electron delocalization. Bader charge calculations[71] revealed that NO_2^- chemisorption is more favorable on the metastable 1T-MoS_2, with an average charge transfer of $-0.86e$, compared to $-0.79e$ on 2H-MoS_2. Furthermore, Figure 4b compares the densities of states (DOS) of 1T-MoS_2 and 2H-MoS_2, showing that the d-band center position of 1T-MoS_2 (ε_{d2} = −3.99 eV) is closer to the Fermi level (E_F) than that of 2H-MoS_2 (ε_{d2} = −4.17 eV), which favors NO_2^- adsorption. The partial density of states also indicates that 1T-MoS_2 has a larger overlap of the Mo d valence orbitals with the N p valence orbitals than 2H-MoS_2 (Figure S18), suggesting that 1T-MoS_2 has more occupied Mo orbitals and a stronger binding with N atoms from adsorbates such as NO_2^-.

We also investigated various adsorption sites of NO_2^- and H^+ on N-MoS_2, including Mo top distal (TD), Mo−Mo bridge distal (BD), Mo with N-doped sites (ND), and Mo with S vacancy sites (SV) (Figure S19). We found that eNO_2^-RR is inhibited on VGs due to the extremely high adsorption energy (1.54 eV; Table S3). As shown in the Gibbs free energy diagrams of HER in Figure 4c, compared to the adsorption sites for pristine MoS_2 ($\Delta G^*_{BD}H$ = −0.06 eV and $\Delta G^*_{TD}H$ = 0.02 eV), N-doped sites and S vacancy sites in N-MoS_2 ($\Delta G^*_{ND}H$ = 1.17 eV and $\Delta G^*_{SV}H$ = 0.41 eV) yield higher energy barriers, confirming that the enhanced eNO_2^-RR selectivity correlates with the suppression of HER. Importantly, the free energy changes of the eNO_2^-RR pathways at different adsorption sites (Figure 4d; see Figures S21−S25 for more details) indicate that the energy barrier of the potential-determining step (PDS) for eNO_2^-RR in N-doped MoS_2 (ΔG^{PDS}_{ND} = 0.43 eV and ΔG^{PDS}_{SV} = 0.68 eV) exhibits significantly better eNO_2^-RR preference than MoS_2 (ΔG^{PDS}_{TD} = 1.19 eV and ΔG^{PDS}_{BD} = 1.67 eV). These findings lead us to conclude that 1T-MoS_2 facilitates stronger binding and faster electron transfer and that Mo with N doping and S vacancies is beneficial for NH_3 synthesis.

The optimal energy cost of the system is 1.41 MJ $mol_{NH_3}^{-1}$ for plasma NO_x generation and 0.99 MJ $mol_{NH_3}^{-1}$ for eNO_2^-RR, yielding a total energy cost of 2.4 MJ $mol_{NH_3}^{-1}$. This corresponds to a total of 39.2 kWh $kg_{NH_3}^{-1}$, which is at least 24.5% lower than that of the state-of-the-art plasma electrocatalysis systems (Table S7). Moreover, the proposed system has the potential to be extended to a cascade system by coupling plasma with multistage electrocatalyst cells, which can be powered flexibly by intermittent renewable electricity (Tables S8 and S9).

CONCLUSIONS

In summary, we have developed a plasma tandem-electrocatalysis system for NH_3 synthesis directly from air, achieving an impressive NH_3 production rate of 7.3 mg h^{-1} cm^{-2} at −0.53 V vs RHE. We engineered a novel defective N-MoS_2/VGs electrocatalyst, which incorporates metallic 1T-MoS_2 phase, N doping, and S vacancies through a one-step plasma engraving process. Experimental and DFT investigations confirmed the crucial role of plasma engraving in catalyst

https://doi.org/10.1021/jacsau.3c00087
JACS Au 2023, 3, 1328−1336

fabrication. The adsorption sites of Mo with N doping and S vacancies possess a lower energy barrier for PDS for NH_3 formation than for H_2 generation, explaining the enhanced eNO_2^-RR performance. This system provides a carbon-free and sustainable approach to NH_3 synthesis with an enhanced production rate. It also serves as a promising solution for chemical storage of carbon-neutral fuels with high location and scale flexibility, adapting readily to the irregular supply of renewable electricity.

EXPERIMENTAL SECTION

Plasma Tandem-Electrocatalysis Setup

The plasma tandem-electrocatalysis system used in this study is schematically shown in Figure S1. A small-scale atmospheric gliding arc plasma (GAP) reactor was designed to generate NO_x from air. The reactor consisted of a stainless steel inner anode rod with a diameter of 4 mm and a length of 58 mm and an outer cathode shell (grounded) with a convergent nozzle having a diameter of 21 mm and a thickness of 7.5 mm. The plasma discharge was powered by an AC high voltage power supply (GK-10020L). Dry air was fed into the reactor at a flow rate of 9 L min^{-1}, which was controlled by a mass flow controller (MFC, TJ-700C). The arc was ignited at the narrowest gap (kept at 1 mm). The GAP reactor had three radial gas inlets to create more intense flow disturbances inside the reactor, allowing for the formation of an extended plasma area. The reactive plasma system effectively activated the nitrogen bond, leading to the formation of NO_x. To quantify the NO_x produced with high concentration (NO and NO_2), the outlet gas was diluted with pure nitrogen and measured using a gas analyzer (MRU VARIO). The generated NO_x was continuously fed into the electroreduction cells (single or tandem) for 1 h, absorbed by the alkaline electrolyte, and catalyzed into NH_3.

Catalyst Synthesis

VG arrays were first prepared using an RF PECVD method powered by a high-frequency generator (Kmate, HERO-500 W, 13.56 MHz). A piece of CC was used as the substrate and thoroughly rinsed before use. First, the CC was placed in a quartz tube with a diameter of 48 mm and a length of 1000 mm, and the entire process was carried out under low-pressure conditions (~0.5 Torr), which is vital for the growth of graphene. Subsequently, a mixed gas of methane (CH_4), hydrogen (H_2), and argon (Ar) was then introduced at a total flow rate of 35 mL min^{-1} (CH_4: 20 mL min^{-1}; H_2: 5 mL min^{-1}; Ar: 10 mL min^{-1}). The RF plasma was generated at 500 W for 10 min, resulting in the decoration on the CC substrate.

MoS_2 nanosheets were fabricated using a conventional hydrothermal method. The VGs obtained were immersed in a homogeneous solution containing 4.8 mmol of $Na_2MoO_4{\cdot}2H_2O$ (sodium molybdate dihydrate), 20 mmol of CH_3CSNH_2 (thioacetamide), and 80 mL of deionized water after vigorous stirring for 30 min. Then the mixture was transferred to a Teflon-lined autoclave, and the temperature was maintained at 200 °C for 12 h. The obtained sample was then annealed at 300 °C to obtain MoS_2/VG arrays. The MoS_2/VGs sample was further treated with RF plasma under an NH_3 atmosphere at a flow rate of 40 mL min^{-1} for 20 min to obtain N-MoS_2/VGs.

Catalyst Characterizations

Field-emission SEM images were recorded using a Hitachi SU8010. TEM images, EDX elemental mappings, and a SAED pattern were collected using a JEOL 2100F microscope. HAADF images were collected using a JEM-ARM200F microscope. XRD patterns were obtained using Cu Kα radiation on a Rigaku D/Max-2550 diffractometer. Raman spectra were collected using a Renishaw-in Via Raman microscope with 514 nm laser excitation. XPS was obtained using an ESCALAB_250Xi X-ray photoelectron spectrometer. Specific surface area distributions were determined using a JW-BK112 analyzer. EPR spectra were taken using a JES FA-200 continuous-wave spectrometer with a sweeping magnetic field and an X band (9.2 GHz) at room temperature. Details of these methods are available in SI.

ASSOCIATED CONTENT

Supporting Information

The Supporting Information is available free of charge at https://pubs.acs.org/doi/10.1021/jacsau.3c00087.

Additional experimental details and methods; energy consumption calculations; phase transformation and kinetic enhancement enabled by plasma engraving; calibration curves of NH_4^+ and N_2H_4 and ^1H NMR spectra, chronoamperometry curves, UV−vis absorption spectra, and NRR performance for each reaction; morphology of the catalyst before and after stability tests; ammonia quantification by ^{15}N and ^{14}N isotope labeling; DFT calculation details; energy consumption comparison of plasma NO_x generation and eNO_2-RR; summary of reported ammonia syntheses in conventional eNRR and plasma tandem-electrocatalysis systems; and summary of reported solar-powered plasma setups and solar-driven electrocatalysis and tables of performance comparison (PDF)

AUTHOR INFORMATION

Corresponding Authors

Hao Zhang − *State Key Laboratory of Clean Energy Utilization, College of Energy and Engineering, Academy of Ecological Civilization, Zhejiang University, Hangzhou 310027, China;* orcid.org/0000-0002-1639-4089; Email: zhang_hao@zju.edu.cn

Shuangyin Wang − *State Key Laboratory of Chem/Bio-Sensing and Chemometrics, College of Chemistry and Chemical Engineering, Hunan University, Changsha 410082, China;* orcid.org/0000-0001-7185-9857; Email: shuangyinwang@hnu.edu.cn

Xin Tu − *Department of Electrical Engineering and Electronics, University of Liverpool, Liverpool L69 3GJ, U.K.;* orcid.org/0000-0002-6376-0897; Email: xin.tu@liv.ac.uk

Annemie Bogaerts − *Research Group PLASMANT, Department of Chemistry, University of Antwerp, BE-2610 Wilrijk, Belgium;* orcid.org/0000-0001-9875-6460; Email: annemie.bogaerts@uantwerpen.be

Authors

Jiageng Zheng − *State Key Laboratory of Clean Energy Utilization, College of Energy and Engineering, Academy of Ecological Civilization, Zhejiang University, Hangzhou 310027, China*

Jiabao Lv − *State Key Laboratory of Clean Energy Utilization, College of Energy and Engineering, Academy of Ecological Civilization, Zhejiang University, Hangzhou 310027, China*

Meng Zhang − *College of Optical Science and Engineering, Zhejiang University, Hangzhou 310027, China*

Jieying Wan − *State Key Laboratory of Clean Energy Utilization, College of Energy and Engineering, Academy of Ecological Civilization, Zhejiang University, Hangzhou 310027, China*

Nick Gerrits − *Research Group PLASMANT, Department of Chemistry, University of Antwerp, BE-2610 Wilrijk, Belgium*

Angjian Wu − *State Key Laboratory of Clean Energy Utilization, College of Energy and Engineering, Academy of*

https://doi.org/10.1021/jacsau.3c00087
JACS Au 2023, 3, 1328−1336

Ecological Civilization, Zhejiang University, Hangzhou 310027, China; orcid.org/0000-0002-0172-7207

Bingru Lan − *State Key Laboratory of Clean Energy Utilization, College of Energy and Engineering, Academy of Ecological Civilization, Zhejiang University, Hangzhou 310027, China*

Weitao Wang − *Department of Electrical Engineering and Electronics, University of Liverpool, Liverpool L69 3GJ, U.K.*

Xiaodong Li − *State Key Laboratory of Clean Energy Utilization, College of Energy and Engineering, Academy of Ecological Civilization, Zhejiang University, Hangzhou 310027, China;* orcid.org/0000-0002-5331-5968

Complete contact information is available at: https://pubs.acs.org/10.1021/jacsau.3c00087

Author Contributions

#J.Z. and H.Z. contributed equally. CRediT: **Jiageng Zheng** formal analysis, investigation, writing-original draft; **Hao Zhang** conceptualization, formal analysis, supervision, writing-original draft, writing-review & editing; **Jiabao Lv** formal analysis, investigation, writing-original draft; **Meng Zhang** validation, writing-review & editing; **Jieying Wan** investigation, validation; **Nick Gerrits** formal analysis, investigation, validation, writing-review & editing; **Angjian Wu** validation; **Bingru Lan** investigation; **Weitao Wang** formal analysis, investigation, validation; **Shuangyin Wang** supervision, writing-review & editing; **Xin Tu** conceptualization, project administration, supervision, writing-review & editing; **Annemie Bogaerts** supervision, writing-review & editing; **Xiaodong Li** conceptualization, funding acquisition, project administration, supervision, writing-review & editing.

Notes

The authors declare no competing financial interest.

■ ACKNOWLEDGMENTS

This work was supported by the National Natural Science Foundation of China (51976191, 5227060056, 52276214) and the National Key Technologies R&D Program of China (2018YFE0117300). N.G. was financially supported through an NWO Rubicon Grant (019.202EN.012). X.T. acknowledges the support of the Engineering and Physical Sciences Research Council (EP/X002713/1).

■ REFERENCES

(1) Chen, J. G.; Crooks, R. M.; Seefeldt, L. C.; Bren, K. L.; Bullock, R. M.; Darensbourg, M. Y.; Holland, P. L.; Hoffman, B.; Janik, M. J.; Jones, A. K.; et al. Beyond fossil fuel-driven nitrogen transformations. *Science* **2018**, *360*, eaar6611.

(2) Service, R. F. New recipe produces ammonia from air, water, and sunlight. *Science* **2014**, *345*, 610.

(3) Hu, X.; Sun, Y.; Guo, S.; Sun, J.; Fu, Y.; Chen, S.; Zhang, S.; Zhu, J. Identifying electrocatalytic activity and mechanism of $Ce_{1/3}NbO_3$ perovskite for nitrogen reduction to ammonia at ambient conditions. *Appl. Catal., B* **2021**, *280*, 119419.

(4) Schlögl, R. Catalytic Synthesis of Ammonia—A "Never-Ending Story"? *Angew. Chem., Int. Ed.* **2003**, *42*, 2004−2008.

(5) Ertl, G. Reactions at Surfaces: From Atoms to Complexity (Nobel Lecture). *Angew. Chem., Int. Ed.* **2008**, *47*, 3524−3535.

(6) van der Ham, C. J. M.; Koper, M. T. M.; Hetterscheid, D. G. H. Challenges in reduction of dinitrogen by proton and electron transfer. *Chem. Soc. Rev.* **2014**, *43*, 5183−5191.

(7) Wang, Q.; Lei, Y.; Wang, D.; Li, Y. Defect engineering in earth-abundant electrocatalysts for CO_2 and N_2 reduction. *Energy Environ. Sci.* **2019**, *12*, 1730−1750.

(8) Zhao, S.; Lu, X.; Wang, L.; Gale, J.; Amal, R. Carbon-Based Metal-Free Catalysts for Electrocatalytic Reduction of Nitrogen for Synthesis of Ammonia at Ambient Conditions. *Adv. Mater.* **2019**, *31*, 1805367.

(9) Chang, B.; Deng, L.; Wang, S.; Shi, D.; Ai, Z.; Jiang, H.; Shao, Y.; Zhang, L.; Shen, J.; Wu, Y.; et al. A vanadium-nickel oxynitride layer for enhanced electrocatalytic nitrogen fixation in neutral media. *J. Mater. Chem. A* **2020**, *8*, 91−96.

(10) Arif, M.; Yasin, G.; Luo, L.; Ye, W.; Mushtaq, M. A.; Fang, X.; Xiang, X.; Ji, S.; Yan, D. Hierarchical hollow nanotubes of NiFeV-layered double hydroxides@CoVP heterostructures towards efficient, pH-universal electrocatalytical nitrogen reduction reaction to ammonia. *Appl. Catal., B* **2020**, *265*, 118559.

(11) Mulder, F. M. Implications of diurnal and seasonal variations in renewable energy generation for large scale energy storage. *J. Renewable Sustainable Energy* **2014**, *6*, 033105.

(12) Bao, D.; Zhang, Q.; Meng, F.; Zhong, H.; Shi, M.; Zhang, Y.; Yan, J.; Jiang, Q.; Zhang, X. Electrochemical Reduction of N_2 under Ambient Conditions for Artificial N_2 Fixation and Renewable Energy Storage Using N_2/NH_3 Cycle. *Adv. Mater.* **2017**, *29*, 1604799.

(13) Kugler, K.; Luhn, M.; Schramm, J. A.; Rahimi, K.; Wessling, M. Galvanic deposition of Rh and Ru on randomly structured Ti felts for the electrochemical NH_3 synthesis. *Phys. Chem. Chem. Phys.* **2015**, *17*, 3768−3782.

(14) Chen, S.; Perathoner, S.; Ampelli, C.; Mebrahtu, C.; Su, D.; Centi, G. Electrocatalytic Synthesis of Ammonia at Room Temperature and Atmospheric Pressure from Water and Nitrogen on a Carbon-Nanotube-Based Electrocatalyst. *Angew. Chem., Int. Ed.* **2017**, *56*, 2699−2703.

(15) Liu, Q.; Zhang, X.; Zhang, B.; Luo, Y.; Cui, G.; Xie, F.; Sun, X. Ambient N_2 fixation to NH_3 electrocatalyzed by a spinel Fe_3O_4 nanorod. *Nanoscale* **2018**, *10*, 14386−14389.

(16) Qiu, W.; Xie, X.; Qiu, J.; Fang, W.; Liang, R.; Ren, X.; Ji, X.; Cui, G.; Asiri, A. M.; Cui, G.; et al. High-performance artificial nitrogen fixation at ambient conditions using a metal-free electrocatalyst. *Nat. Commun.* **2018**, *9*, 3485.

(17) Chang, B.; Li, L.; Shi, D.; Jiang, H.; Ai, Z.; Wang, S.; Shao, Y.; Shen, J.; Wu, Y.; Li, Y.; et al. Metal-free boron carbonitride with tunable boron Lewis acid sites for enhanced nitrogen electroreduction to ammonia. *Appl. Catal., B* **2021**, *283*, 119622.

(18) Huang, Y.; Yang, T.; Yang, L.; Liu, R.; Zhang, G.; Jiang, J.; Luo, Y.; Lian, P.; Tang, S. Graphene-boron nitride hybrid-supported single Mo atom electrocatalysts for efficient nitrogen reduction reaction. *J. Mater. Chem. A* **2019**, *7*, 15173−15180.

(19) Sippel, D.; Rohde, M.; Netzer, J.; Trncik, C.; Gies, J.; Grunau, K.; Djurdjevic, I.; Decamps, L.; Andrade, S. L. A.; Einsle, O. A bound reaction intermediate sheds light on the mechanism of nitrogenase. *Science* **2018**, *359*, 1484−1489.

(20) Hoffman, B. M.; Lukoyanov, D.; Yang, Z.; Dean, D. R.; Seefeldt, L. C. Mechanism of Nitrogen Fixation by Nitrogenase: The Next Stage. *Chem. Rev.* **2014**, *114*, 4041−4062.

(21) Stiefel, E. I. Proposed Molecular Mechanism for the Action of Molybdenum in Enzymes: Coupled Proton and Electron Transfer. *Proc. Natl. Acad. Sci. U. S. A.* **1973**, *70*, 988−992.

(22) Lin, G.; Ju, Q.; Guo, X.; Zhao, W.; Adimi, S.; Ye, J.; Bi, Q.; Wang, J.; Yang, M.; Huang, F. Intrinsic Electron Localization of Metastable MoS_2 Boosts Electrocatalytic Nitrogen Reduction to Ammonia. *Adv. Mater.* **2021**, *33*, 2007509.

(23) Zhao, X.; Zhang, X.; Xue, Z.; Chen, W.; Zhou, Z.; Mu, T. Fe nanodot-decorated MoS_2 nanosheets on carbon cloth: an efficient and flexible electrode for ambient ammonia synthesis. *J. Mater. Chem. A* **2019**, *7*, 27417−27422.

(24) Zi, X.; Wan, J.; Yang, X.; Tian, W.; Zhang, H.; Wang, Y. Vacancy-rich 1T-MoS_2 monolayer confined to MoO_3 matrix: An interface-engineered hybrid for efficiently electrocatalytic conversion of nitrogen to ammonia. *Appl. Catal., B* **2021**, *286*, 119870.

(25) Cheng, H.; Ding, L.; Chen, G.; Zhang, L.; Xue, J.; Wang, H. Molybdenum Carbide Nanodots Enable Efficient Electrocatalytic Nitrogen Fixation under Ambient Conditions. *Adv. Mater.* **2018**, *30*, 1803694.
(26) Inoue, Y.; Kitano, M.; Kishida, K.; Abe, H.; Niwa, Y.; Sasase, M.; Fujita, Y.; Ishikawa, H.; Yokoyama, T.; Hara, M.; et al. Efficient and Stable Ammonia Synthesis by Self-Organized Flat Ru Nanoparticles on Calcium Amide. *ACS Catal.* **2016**, *6*, 7577−7584.
(27) Liu, Y.; Chen, X.; Yu, J.; Ding, B. Carbon-Nanoplated CoS@TiO_2 Nanofibrous Membrane: An Interface-Engineered Heterojunction for High-Efficiency Electrocatalytic Nitrogen Reduction. *Angew. Chem., Int. Ed.* **2019**, *58*, 18903−18907.
(28) Deng, J.; Iñiguez, J. A.; Liu, C. Electrocatalytic Nitrogen Reduction at Low Temperature. *Joule* **2018**, *2*, 846−856.
(29) Hu, L.; Xing, Z.; Feng, X. Understanding the Electrocatalytic Interface for Ambient Ammonia Synthesis. *ACS Energy Lett.* **2020**, *5*, 430−436.
(30) Sun, J.; Alam, D.; Daiyan, R.; Masood, H.; Zhang, T.; Zhou, R.; Cullen, P. J.; Lovell, E. C.; Jalili, A. R.; Amal, R. A hybrid plasma electrocatalytic process for sustainable ammonia production. *Energy Environ. Sci.* **2021**, *14*, 865−872.
(31) Hollevoet, L.; Jardali, F.; Gorbanev, Y.; Creel, J.; Bogaerts, A.; Martens, J. A. Towards Green Ammonia Synthesis through Plasma-Driven Nitrogen Oxidation and Catalytic Reduction. *Angew. Chem., Int. Ed.* **2020**, *59*, 23825−23829.
(32) Hollevoet, L.; Vervloessem, E.; Gorbanev, Y.; Nikiforov, A.; De Geyter, N.; Bogaerts, A.; Martens, J. A. Energy-Efficient Small-Scale Ammonia Synthesis Process with Plasma-Enabled Nitrogen Oxidation and Catalytic Reduction of Adsorbed NO_x. *ChemSusChem* **2022**, *15*, No. e202102526.
(33) Kani, N. C.; Gauthier, J. A.; Prajapati, A.; Edgington, J.; Bordawekar, I.; Shields, W.; Shields, M.; Seitz, L. C.; Singh, A. R.; Singh, M. R. Solar-driven electrochemical synthesis of ammonia using nitrate with 11% solar-to-fuel efficiency at ambient conditions. *Energy Environ. Sci.* **2021**, *14*, 6349−6359.
(34) Nagassou, D.; Mohsenian, S.; Bhatta, S.; Elahi, R.; Trelles, J. P. Solar-gliding arc plasma reactor for carbon dioxide decomposition: Design and characterization. *Sol. Energy* **2019**, *180*, 678−689.
(35) Bogaerts, A.; Neyts, E. C. Plasma Technology: An Emerging Technology for Energy Storage. *ACS Energy Lett.* **2018**, *3*, 1013−1027.
(36) Li, L.; Tang, C.; Cui, X.; Zheng, Y.; Wang, X.; Xu, H.; Zhang, S.; Shao, T.; Davey, K.; Qiao, S. Efficient Nitrogen Fixation to Ammonia through Integration of Plasma Oxidation with Electrocatalytic Reduction. *Angew. Chem., Int. Ed.* **2021**, *60*, 14131−14137.
(37) Wu, A.; Yang, J.; Xu, B.; Wu, X.; Wang, Y.; Lv, X.; Ma, Y.; Xu, A.; Zheng, J.; Tan, Q.; et al. Direct ammonia synthesis from the air via gliding arc plasma integrated with single atom electrocatalysis. *Appl. Catal., B* **2021**, *299*, 120667.
(38) Deng, S.; Luo, M.; Ai, C.; Zhang, Y.; Liu, B.; Huang, L.; Jiang, Z.; Zhang, Q.; Gu, L.; Lin, S.; et al. Synergistic Doping and Intercalation: Realizing Deep Phase Modulation on MoS2 Arrays for High-Efficiency Hydrogen Evolution Reaction. *Angew. Chem., Int. Ed.* **2019**, *58*, 16289−16296.
(39) Paraknowitsch, J. P.; Thomas, A. Doping carbons beyond nitrogen: an overview of advanced heteroatom doped carbons with boron, sulphur and phosphorus for energy applications. *Energy Environ. Sci.* **2013**, *6*, 2839−2855.
(40) Jiang, Q.; Chen, N.; Liu, D.; Wang, S.; Zhang, H. Efficient plasma-enhanced method for layered $LiNi_{1/3}Co_{1/3}Mn_{1/3}O_2$ cathodes with sulfur atom-scale modification for superior-performance Li-ion batteries. *Nanoscale* **2016**, *8*, 11234−11240.
(41) Ouyang, B.; Zhang, Y.; Wang, Y.; Zhang, Z.; Fan, H. J.; Rawat, R. S. Plasma surface functionalization induces nanostructuring and nitrogen-doping in carbon cloth with enhanced energy storage performance. *J. Mater. Chem. A* **2016**, *4*, 17801−17808.
(42) Fang, Y.; Hu, X.; Zhao, W.; Pan, J.; Wang, D.; Bu, K.; Mao, Y.; Chu, S.; Liu, P.; Zhai, T.; et al. Structural Determination and Nonlinear Optical Properties of New 1T‴-Type MoS_2 Compound. *J. Am. Chem. Soc.* **2019**, *141*, 790−793.
(43) Yu, Y.; Nam, G.; He, Q.; Wu, X.; Zhang, K.; Yang, Z.; Chen, J.; Ma, Q.; Zhao, M.; Liu, Z.; et al. High phase-purity 1T′-MoS_2- and 1T′-$MoSe_2$-layered crystals. *Nat. Chem.* **2018**, *10*, 638−643.
(44) Shang, C.; Lei, B.; Zhuo, W. Z.; Zhang, Q.; Zhu, C. S.; Cui, J. H.; Luo, X. G.; Wang, N. Z.; Meng, F. B.; Ma, L. K.; et al. Structural and electronic phase transitions driven by electric field in metastable MoS_2 thin flakes. *Phys. Rev. B* **2019**, *100*, 020508.
(45) Morales-Guio, C. G.; Hu, X. Amorphous Molybdenum Sulfides as Hydrogen Evolution Catalysts. *Acc. Chem. Res.* **2014**, *47*, 2671−2681.
(46) Belanger, D.; Laperriere, G.; Girard, F.; Guay, D.; Tourillon, G. Physicochemical characteristics of electrochemically deposited molybdenum sulfide and polypyrrole-tetrathiomolybdate/molybdenum trisulfide composite electrodes. *Chem. Mater.* **1993**, *5*, 861−868.
(47) González, J. R.; Alcántara, R.; Tirado, J. L.; Fielding, A. J.; Dryfe, R. A. W. Electrochemical Interaction of Few-Layer Molybdenum Disulfide Composites vs Sodium: New Insights on the Reaction Mechanism. *Chem. Mater.* **2017**, *29*, 5886−5895.
(48) Xu, X.; Liu, X.; Zhao, J.; Wu, D.; Du, Y.; Yan, T.; Zhang, N.; Ren, X.; Wei, Q. Interface engineering of MoS_2@$Fe(OH)_3$ nanoarray heterostucture: Electrodeposition of MoS_2@$Fe(OH)_3$ as N_2 and H^+ channels for artificial NH_3 synthesis under mild conditions. *J. Colloid Interface Sci.* **2022**, *606*, 1374−1379.
(49) Wang, C.; Yang, M.; Wang, X.; Ma, H.; Tian, Y.; Pang, H.; Tan, L.; Gao, K. Hierarchical CoS_2/MoS_2 flower-like heterostructured arrays derived from polyoxometalates for efficient electrocatalytic nitrogen reduction under ambient conditions. *J. Colloid Interface Sci.* **2022**, *609*, 815−824.
(50) Duan, J.; Shao, D.; He, X.; Lu, Y.; Wang, W. Model MoS_2@ZIF-71 interface acts as a highly active and selective electrocatalyst for catalyzing ammonia synthesis. *Colloids Surf., A* **2021**, *619*, 126529.
(51) Jiang, T.; Li, L.; Li, L.; Liu, Y.; Zhang, D.; Zhang, D.; Li, H.; Mao, B.; Shi, W. Ultra-thin shelled $Cu_{2-x}S$/MoS_2 quantum dots for enhanced electrocatalytic nitrogen reduction. *Chem. Eng. J.* **2021**, *426*, 130650.
(52) Guo, Y.; Yao, Z.; Timmer, B. J. J.; Sheng, X.; Fan, L.; Li, Y.; Zhang, F.; Sun, L. Boosting nitrogen reduction reaction by bio-inspired FeMoS containing hybrid electrocatalyst over a wide pH range. *Nano Energy* **2019**, *62*, 282−288.
(53) Matanovic, I.; Leung, K.; Percival, S. J.; Park, J. E.; Lu, P.; Atanassov, P.; Chou, S. S. Towards defect engineering in hexagonal MoS_2 nanosheets for tuning hydrogen evolution and nitrogen reduction reactions. *Appl. Mater. Today* **2020**, *21*, 100812.
(54) Mao, H.; Fu, Y.; Yang, H.; Deng, Z.; Sun, Y.; Liu, D.; Wu, Q.; Ma, T.; Song, X. Ultrathin 1T-MoS_2 Nanoplates Induced by Quaternary Ammonium-Type Ionic Liquids on Polypyrrole/Graphene Oxide Nanosheets and Its Irreversible Crystal Phase Transition During Electrocatalytic Nitrogen Reduction. *ACS Appl. Mater. Interfaces* **2020**, *12*, 25189−25199.
(55) Yang, G.; Zhao, L.; Huang, G.; Liu, Z.; Yu, S.; Wang, K.; Yuan, S.; Sun, Q.; Li, X.; Li, N. Electrochemical Fixation of Nitrogen by Promoting N_2 Adsorption and N-N Triple Bond Cleavage on the CoS_2/MoS_2 Nanocomposite. *ACS Appl. Mater. Interfaces* **2021**, *13*, 21474−21481.
(56) Yang, M.; Jin, Z.; Wang, C.; Cao, X.; Wang, X.; Ma, H.; Pang, H.; Tan, L.; Yang, G. Fe Foam-Supported FeS_2-MoS_2 Electrocatalyst for N2 Reduction under Ambient Conditions. *ACS Appl. Mater. Interfaces* **2021**, *13*, 55040−55050.
(57) Ye, W.; Arif, M.; Fang, X.; Mushtaq, M. A.; Chen, X.; Yan, D. Efficient Photoelectrochemical Route for the Ambient Reduction of N_2 to NH_3 Based on Nanojunctions Assembled from MoS_2 Nanosheets and TiO_2. *ACS Appl. Mater. Interfaces* **2019**, *11*, 28809−28817.
(58) Chu, K.; Liu, Y.; Li, Y.; Guo, Y.; Tian, Y. Two-dimensional (2D)/2D Interface Engineering of a MoS_2/C_3N_4 Heterostructure for Promoted Electrocatalytic Nitrogen Fixation. *ACS Appl. Mater. Interfaces* **2020**, *12*, 7081−7090.

https://doi.org/10.1021/jacsau.3c00087
JACS Au 2023, 3, 1328−1336

(59) Suryanto, B. H. R.; Wang, D.; Azofra, L. M.; Harb, M.; Cavallo, L.; Jalili, R.; Mitchell, D. R. G.; Chatti, M.; MacFarlane, D. R. MoS_2 Polymorphic Engineering Enhances Selectivity in the Electrochemical Reduction of Nitrogen to Ammonia. *ACS Energy Lett.* **2019**, *4*, 430−435.
(60) Zhao, Z.; Luo, S.; Ma, P.; Luo, Y.; Wu, W.; Long, Y.; Ma, J. In Situ Synthesis of MoS_2 on C_3N_4 To Form MoS_2/C_3N_4 with Interfacial Mo-N Coordination for Electrocatalytic Reduction of N_2 to NH_3. *ACS Sustainable Chem. Eng.* **2020**, *8*, 8814−8822.
(61) Liu, Y.; Wang, W.; Zhang, S.; Li, W.; Wang, G.; Zhang, Y.; Han, M.; Zhang, H. MoS_2 Nanodots Anchored on Reduced Graphene Oxide for Efficient N_2 Fixation to NH_3. *ACS Sustainable Chem. Eng.* **2020**, *8*, 2320−2326.
(62) Zhang, L.; Ji, X.; Ren, X.; Ma, Y.; Shi, X.; Tian, Z.; Asiri, A. M.; Chen, L.; Tang, B.; Sun, X. Electrochemical Ammonia Synthesis via Nitrogen Reduction Reaction on a MoS_2 Catalyst: Theoretical and Experimental Studies. *Adv. Mater.* **2018**, *30*, 1800191.
(63) Liu, R.; Guo, T.; Fei, H.; Wu, Z.; Wang, D.; Liu, F. Highly Efficient Electrocatalytic N_2 Reduction to Ammonia over Metallic 1T Phase of MoS_2 Enabled by Active Sites Separation Mechanism. *Adv. Sci.* **2022**, *9*, 2103583.
(64) Zeng, L.; Chen, S.; van der Zalm, J.; Li, X.; Chen, A. Sulfur vacancy-rich N-doped MoS_2 nanoflowers for highly boosting electrocatalytic N_2 fixation to NH_3 under ambient conditions. *Chem. Commun.* **2019**, *55*, 7386−7389.
(65) Liu, B.; Ma, C.; Liu, D.; Yan, S. Sulfur-Vacancy Defective MoS_2 as a Promising Electrocatalyst for Nitrogen Reduction Reaction under Mild Conditions. *ChemElectroChem* **2021**, *8*, 3030−3039.
(66) Fang, B.; Yao, J.; Zhang, X.; Ma, L.; Ye, Y.; Tang, J.; Zou, G.; Zhang, J.; Jiang, L.; Sun, Y. A large scaled-up monocrystalline 3R MoS_2 electrocatalyst for efficient nitrogen reduction reactions. *New J. Chem.* **2021**, *45*, 2488−2495.
(67) Liang, J.; Ma, S.; Li, J.; Wang, Y.; Wu, J.; Zhang, Q.; Liu, Z.; Yang, Z.; Qu, K.; Cai, W. Boosting the acidic electrocatalytic nitrogen reduction performance of MoS_2 by strain engineering. *J. Mater. Chem. A* **2020**, *8*, 10426−10432.
(68) Patil, S. B.; Chou, H.; Chen, Y.; Hsieh, S.; Chen, C.; Chang, C.; Li, S.; Lee, Y.; Lin, Y.; Li, H.; et al. Enhanced N_2 affinity of 1T-MoS_2 with a unique pseudo-six-membered ring consisting of N-Li-S-Mo-S-Mo for high ambient ammonia electrosynthesis performance. *J. Mater. Chem. A* **2021**, *9*, 1230−1239.
(69) Luo, Y.; Shen, P.; Li, X.; Guo, Y.; Chu, K. MoS_2 quantum dots for electrocatalytic N_2 reduction. *Chem. Commun.* **2021**, *57*, 9930−9933.
(70) Xu, X.; Wang, Y.; Chen, X.; Qian, X.; Liang, Z.; Cui, H.; Tian, J.; Shao, M. Semi-metal 1T′ phase MoS_2 nanosheets for promoted electrocatalytic nitrogen reduction. *EcoMat* **2021**, *3*, No. e12122.
(71) Henkelman, G.; Arnaldsson, A.; Jónsson, H. A fast and robust algorithm for Bader decomposition of charge density. *Comput. Mater. Sci.* **2006**, *36*, 354−360.

https://doi.org/10.1021/jacsau.3c00087
JACS Au 2023, 3, 1328−1336